

Contents lists available at ScienceDirect

Chaos, Solitons and Fractals

journal homepage: www.elsevier.com/locate/chaos



Non-autonomous standard nontwist map

Marcos V. de Moraes a,b, Iberê L. Caldas a, Yves Elskens b

- ^a Institute of Physics, University of São Paulo, Rua do Matão 1371, São Paulo, SP, 05508-090, Brazil ^b Aix-Marseille Université, UMR 7345 CNRS, PIIM, 52 Av. Escadrille Normandie Niemen, Marseille, 13397 cedex 20, France

ARTICLE INFO

Keywords: Hamiltonian modeling Non-autonomous systems Transport barriers

ABSTRACT

Area-preserving nontwist maps locally violate the twist condition, giving rise to shearless curves. Nontwist systems appear in different physical contexts, such as plasma physics, climate physics, classical mechanics, etc. Generic properties of nontwist maps are captured by the standard nontwist map, which depends on a convection parameter a and a modulation coefficient b. In the spirit of non-autonomous systems, we consider the standard nontwist map (SNM) with a linearly increasing modulation coefficient, and we investigate the evolution of an ensemble of points on the phase space that initially lie on the shearless invariant curve in the initial state, called shearless snapshot torus. Differently from the SNM with constant parameters — where we can see different scenarios of collision/annihilation of periodic orbits leading to global transport, depending on the region in the parameter space — for the SNM with time-dependent parameters, the route to chaos is not only related to the path in the (a, b) parameter space, but also to the scenario of the evolution of parameter b_n . In this work, we identify power-law relationships between key parameters for the chaotic transition and the iteration time. Additionally, we analyze system reversibility during the chaotic transition and demonstrate an extra transport, where parameter variation modifies the diffusion coefficient.

1. Introduction

In Hamiltonian systems, trajectories in phase space evolve under the influence of Hamilton's equations, which describe the dynamics of canonical coordinates and momenta [1]. Hamiltonian dynamics extends beyond familiar systems, not only well-known conservative ones such as the pendulum [2] but also more complex applications, for example, in the study of transport in plasma physics, fluid dynamics, condensed matter, celestial mechanics and other areas [3-8].

The dynamics of a time-independent Hamiltonian system with Ndegrees of freedom can be visualized in the 2N-dimensional phase space of coordinates and momenta. From an initial value of coordinates and momenta, one can study the dynamics by looking at the trajectory evolution in the phase space. However, finding trajectories in the phase space may be very difficult, as Hamilton's equations are usually not analytically solvable, and numerical solutions might be quite CPUconsuming. One way to simplify the issue is to examine the Poincaré section of the system. For instance, a three-dimensional Hamiltonian system can be analyzed by observing the values of two variables at the moment the third variable reaches a specific value. The Poincaré section can be represented by discrete-time equations called maps, that can arise naturally in Hamiltonian systems [1].

In the context of Hamiltonian dynamics, non-autonomous systems represent a class of dynamical systems where the governing equations of motion explicitly depend on time. Unlike autonomous systems, where the phase space usually shows the coexistence of regular and chaotic trajectories, non-autonomous Hamiltonian systems exhibit time-varying behaviors that depend on the range of the dynamical parameter and the parameter's evolution scenario [9-11]. These systems find widespread application across diverse fields, including celestial mechanics, plasma physics, and climate sciences.

While nontwist maps have been widely studied [12,13], the bibliography for time-varying effects in them is still scarce. In that sense, non-autonomous Hamiltonian systems pose unique theoretical challenges and opportunities, requiring novel techniques to describe their behavior. For instance, the time dependence in these systems breaks conserved quantities and invariant structures, such as invariant tori and periodic orbits, which are central to understanding the system's

In this paper, we explore the behavior of the shearless transport barrier — a distinctive feature of nontwist systems — under the influence of a time-varying parameter in the standard nontwist map (SNM). Our key findings show that for small variations in this parameter, the evolution of the shearless ensemble closely follows the stationary

^{*} Corresponding author at: Institute of Physics, University of São Paulo, Rua do Matão 1371, São Paulo, SP, 05508-090, Brazil. E-mail address: mvdemoraes@usp.br (M.V.d. Moraes).

shearless curve. However, after certain bifurcations, such as separatrix reconnection, the ensemble diverges from the stationary curve. The chaotic transition of the shearless ensemble is characterized by three critical values: the parameters b_c^- (marking the start) and b_c^+ (marking the end) of the chaotic transition, as well as the instantaneous Lyapunov exponent, measured during the transition. We provide numerical results for these values as a function of the parameter's evolution. Additionally, we qualitatively track the chaotic transition by evaluating the reversibility of the shearless ensemble throughout the process. Finally, we demonstrate the occurrence of an extra diffusion linked to the varying parameter.

The structure of the paper is as follows: Section 2 reviews key properties of the SNM. Section 3 introduces the non-autonomous SNM, incorporating the time-dependent parameter. Section 4 investigates the system's behavior under small time-dependent perturbations. Section 5 focuses on the transition to chaos in the shearless snapshot torus. Section 6 briefly addresses the transport properties of the non-autonomous SNM. Finally, Section 7 presents our conclusions.

2. Standard nontwist map

The standard nontwist map (SNM) is a paradigmatic area-preserving map that locally violates the twist condition (cf. Eq. (3)). The SNM M_0 reads [14]

$$M_0 = \begin{cases} y_{n+1} = y_n - b\sin(2\pi x_n) \\ x_{n+1} = x_n + a(1 - y_{n+1}^2) \end{cases}$$
 (1)

where $a \in [0,1)$ and $b \in \mathbb{R}$, and the domain of the variables is $D := \{(x,y) \mid y \in (-\infty,\infty), \ x \in [-1/2,1/2), \ \text{mod} \ 1\}$. Variable x plays the role of an angle, and we call y a radius for simplicity. The index n represents a discrete time, which is called iteration from here on. The parameter a shapes the rotation number along the y direction, therefore, called convection coefficient. The parameter b represents the amplitude of a radial perturbation, and we called it modulation coefficient.

In general, we can define the rotation number ω of an orbit initiated at the point (x_0,y_0) , when it exists, by

$$\omega(x_0, y_0) = \lim_{n \to \infty} \frac{x_n}{n},\tag{2}$$

where the x variable is lifted to the real numbers.

In particular, if an orbit is periodic, then its rotation number is rational, written as the ratio of two integers $\omega = m/n$. Trajectories with irrational rotation numbers populate densely one-dimensional lines called invariant tori, or more complex objects such as cantori [15].

In the integrable limit, b=0, successive iterations of an orbit result in a straight line that wraps around the x-domain. For $b\neq 0$, some invariant curves are destroyed, resulting in a mixed phase space with chaotic regions, while other invariant tori still exist. Fig. 1 shows the rotation number for both integrable and non-integrable cases. Because the rotation number is nonmonotonic, the twist condition

$$\partial \omega / \partial y \neq 0$$
 (3)

is violated, giving rise to the shearless curve.

As the KAM theorem assumes the twist condition, the problem of motion stability in nontwist systems involves understanding how the shearless curve — the curve where the KAM theorem is not valid — breaks up (see [12,13]).

Because the map can be factored as a product of involutions, we can determine indicator points (IPs); if these points belong to a regular orbit, then the orbit is the shearless curve, and the IPs are located on it. The indicator points for the SNM are [16]

$$\mathbf{z}_0^{(\pm)} = (\pm 1/4, \pm b/2), \quad \mathbf{z}_1^{(\pm)} = (a/2 \pm 1/4, 0).$$
 (4)

Fig. 2 shows typical phase portraits of the SNM for fixed a = 0.345. Because of the twist condition violation, periodic orbits with the same rotation number come in pairs. For the integrable case with

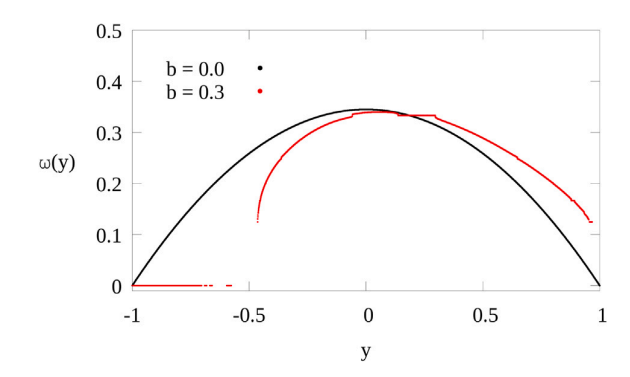


Fig. 1. Rotation number of SNM in function of y coordinate for b=0 (black) and b=0.3 (red). We consider parameter a=0.345. (For interpretation of the references to colour in this figure legend, the reader is referred to the web version of this article.)

a=0.345, two period-3 elliptic orbits are present in the phase space. When $b\neq 0$, the system becomes non-integrable, and the period-3 elliptic orbits transform into island chains separated by a shearless barrier. Additionally, two period-3 hyperbolic points exist in this region, each with its own separatrix. These separatrices eventually collide and reconnect, undergoing a global bifurcation known as separatrix reconnection, which changes the phase space topology from heteroclinic to homoclinic near the shearless curve (see Fig. 3). The separatrix reconnection threshold for period-one orbits may be found analytically, considering that the hyperbolic point in each separatrix will have the same value of the Hamiltonian [12]. For higher-order periodic orbits $(n \geq 2)$, analytical expressions for the reconnection threshold are unavailable. However, our numerical analysis shows that, for a=0.345, separatrix reconnection occurs at $b^*=0.3761$.

For sufficiently high values of the modulation coefficient b (right panel on Fig. 2) almost all invariant curves are destroyed, with the shearless usually being the last one. The critical value of b for shearless torus breakup is, for $a=0.345,\ b_c\approx0.83.$ After this value the shearless torus is destroyed, but there might be still some partial barrier effects [17,18].

3. Parameter drift

This section introduces the non-autonomous standard nontwist map (NASNM). For that, we consider the parameter b in Eq. (1) to be time-dependent

$$b \to b_n$$
. (5)

There are several ways to choose the time dependence. For simplicity, we choose

$$b_n = b_0 + nv, (6)$$

where b_0 is the initial parameter, n is the iteration number and v is the parameter growth rate, written as $v = (b_f - b_0)/N$. The last iteration satisfies the condition $b_N = b_f$, where b_f is the final parameter and N is the total number of iterations. We write $[b_0, b_f, N]$ to denote the drift scenario.

Discrete-time conservative systems are usually considered under the assumption of constant parameters. When parameter drift is introduced, invariant structures like KAM tori are lost, making the analysis of individual trajectories less meaningful. Instead, a more effective approach is to track ensembles that initially correspond to the KAM curves of the original system [9,10]. We define an initial ensemble as a sequence of points \mathbf{r}_i on the phase space lying in an invariant curve

$$\mathbf{R}_0 = \{ \mathbf{r}_0, \mathbf{r}_1, \mathbf{r}_2, \dots, \mathbf{r}_i \}. \tag{7}$$

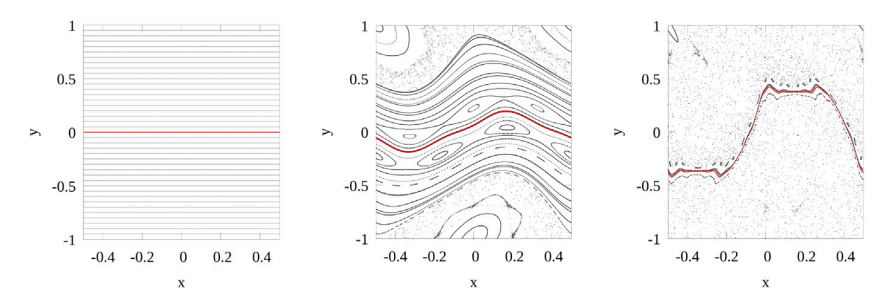


Fig. 2. Phase portraits of the SNM for fixed a = 0.345. On the left the integrable case (b = 0), b = 0.3 on the center, and b = 0.79 on the right. The shearless curve is plotted in red. (For interpretation of the references to colour in this figure legend, the reader is referred to the web version of this article.)

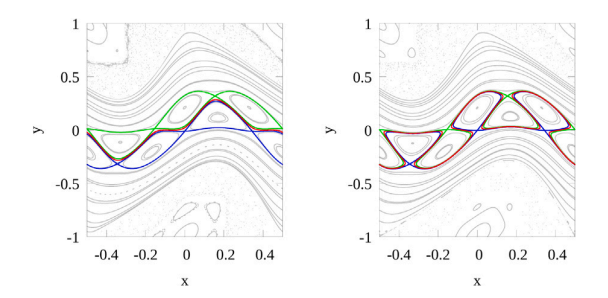


Fig. 3. Phase portraits for the SNM with constant parameters, showing in green (blue) the upper (lower) separatrix and in red the shearless curve. On the left side b=0.37, and on the right b=0.38. (For interpretation of the references to colour in this figure legend, the reader is referred to the web version of this article.)

Considering the shearless invariant torus, for the given fixed b_0 , we choose one of the indicator points $\mathbf{z}_0, \mathbf{z}_1$ as the initial point \mathbf{r}_0 and the successive points $\{\mathbf{r}_1, \mathbf{r}_2, \dots, \mathbf{r}_i\}$ are obtained from the iteration of \mathbf{r}_0 with the SNM with fixed parameter b_0 . The temporal evolution of the ensemble \mathbf{R}_0 is given by the successive application of the NASNM. At each iteration denoted by n, the current image of this ensemble is called snapshot torus. It is essential to distinguish that the snapshot torus, rather than an invariant curve, undergoes this evolution.

Fig. 4 displays a typical snapshot tori evolution, corresponding to the drift scenario $[b_0 = 0.3, b_f = 1.0, N = 100]$. It is clear that introducing time dependence significantly changes the phase portrait. During earlier time intervals, expressly when $b_n = 0.44$, the system still retains some characteristics of the SNM, evidenced by the resemblance of the snapshot tori to the invariant curves observed in the stationary model. However, as the system evolves, for instance, when $b_n = 0.79$, the phase portrait deviates substantially from the stationary model. Notably, while the stationary system has already lost all invariant curves — the shearless invariant curve usually being the last one —, on the time-dependent model the shearless snapshot torus exhibits a different structure, that is affected by various phenomena observed in the stationary model, such as separatrix reconnection, the emergence of small islands, the destruction of primary islands, and the formation of meanders. In this sense, the ensemble preserves a memory of the evolution scenario.

4. Adiabatic variation and separatrix reconnection

Section 3 was dedicated to showing the main concepts arising from the parameter's time dependence. In this section, we show some results for small and slow parameter variations b_n ,

Fig. 5 shows an evolution scenario for an initial condition with $b_0 = 0.0$ and $b_f = 0.3$.

We see that the shearless snapshot torus tends to the shearless curve for the static picture for the end of the evolution $b_f = b$. The slower the

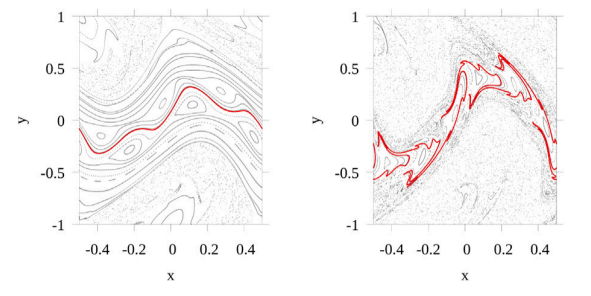


Fig. 4. Snapshots of the non-autonomous SNM for a=0.345 and drift scenario $[b_0=0.3,b_f=1.0,N=100]$, corresponding to the instants n=20 ($b_n=0.44$) on the left, and n=70 ($b_n=0.79$) on the right. The shearless snapshot torus is plotted in red. (For interpretation of the references to colour in this figure legend, the reader is referred to the web version of this article.)

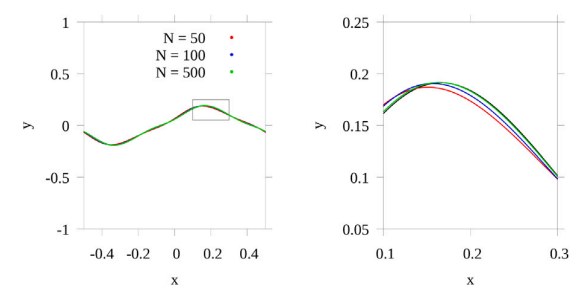


Fig. 5. Shearless invariant curve for b=0.3 in black and the final shearless snapshot torus for the drift scenario $[b_0=0.0,b_f=0.3],\ N=50$ in red, N=100 in blue and N=500 in green, showing that for slower variations of parameter b_n the evolution of NASNM approximates the invariant curves for the static scenario. The right panel shows a close-up of the boxed region in the left panel. (For interpretation of the references to colour in this figure legend, the reader is referred to the web version of this article.)

variation of the parameter b_n , the closer the snapshot torus aligns with its corresponding invariant curve in the static picture.

We quantify this result by calculating the ensemble-averaged rotation number, namely the average rotation number of all ensemble points initially located on the shearless curve. This result is shown in Fig. 6.

We see a very good agreement between the ensemble-averaged rotation number and the rotation number in the static scenario for values of $b_n \leq b^*$. But when the parameter reaches values close to the separatrix reconnection b^* (Fig. 3), the ensemble starts experiencing a stretching towards the separatrix. After that, although the ensemble-averaged rotation number is still close to the rotation number in the static scenario, the phase space is very distinct, notably the standard deviation in Fig. 6.

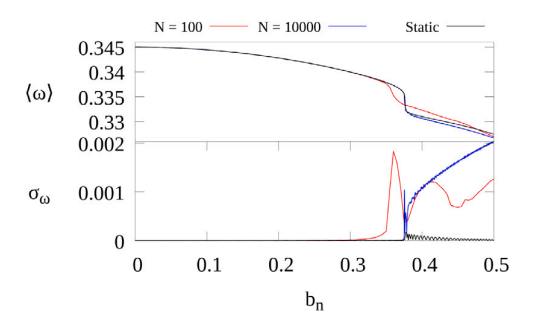


Fig. 6. Averaged rotation number $\langle \omega \rangle$ and the standard deviation σ_{ω} in function of time-dependent parameter b_n . The average is taken over NP=10000 points initially located on the shearless curve for b_0 .

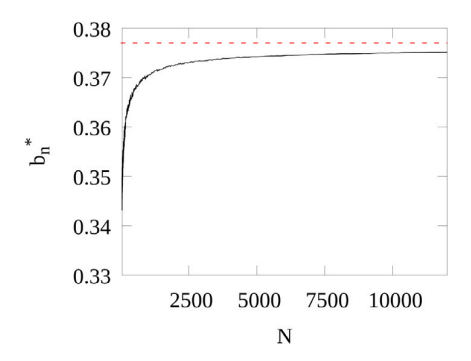


Fig. 7. Critical parameter for separatrix reconnection in function of the total number of iterations.

For the non-autonomous model, we define the separatrix reconnection threshold b_n^* , i.e., the value of b_n where the standard deviation of σ_ω has its maximum value. This result is shown in Fig. 7.

5. Shearless snapshot torus breakup

This section discusses the transition to chaos of the shearless snapshot torus. For stationary Hamiltonian systems, the transition to chaos is usually associated with the destruction of invariant curves. However, with the introduction of parameter drift, there are no longer invariant curves, so the transition to chaos must be studied with different tools and techniques. To address this, we compute the ensemble-averaged pairwise logarithmic distance (EAPLD) given by the expression [19]

$$\rho(n) = \langle \ln d(n) \rangle, \tag{8}$$

where d(n) is the distance between a pair of points very close to each other in the initial state (n=0). The average $\langle \cdot \rangle$ is calculated over an ensemble of NP pairs of points located initially on the invariant shearless curve for the parameters (a,b_0) . Fig. 8 shows a typical evolution scenario as function of the dynamical parameter b_n for fixed $[b_0=0,b_f=2]$ for different numbers of iterations N.

We see a scenario where the distance between the points hardly changes initially. The transition to large-scale chaos begins after a critical parameter b_c^- , where we see an exponentially increasing distance between the points in the ensemble. After the large-scale chaotic transition, for b_c^+ , the ensemble dynamics become strongly chaotic. The chaotic transition of the shearless snapshot torus is now characterized by the critical parameters b_c^- and b_c^+ and the instantaneous Lyapunov exponent λ , which is defined as the slope of the curve during the exponential transition, calculated as function of the discrete-time variable n. The calculated instantaneous Lyapunov exponent λ is unique because it exclusively characterizes the shearless snapshot torus. This parameter

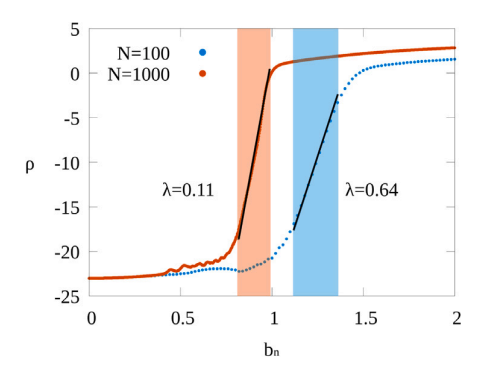


Fig. 8. Ensemble-averaged pairwise logarithmic distance in function of the dynamical parameter b_n for $[b_0=0,b_f=2]$ and NP=50000. In blue N=100, and N=1000 in red. The black fitted lines represent the slope of $\rho(n)$ during chaotic transition, calculated as function of the discrete-time variable n. The colored regions represent the interval b_c^-, b_c^+ for which the chaotic transition occurs. Lambda represents the instantaneous Lyapunov exponent. (For interpretation of the references to colour in this figure legend, the reader is referred to the web version of this article.)

can be ascertained only after a certain duration following the beginning of the chaotic transition.

The critical parameters b_c^- and b_c^+ are determined by identifying the beginning and completion of the exponential transition in the ensemble-averaged pairwise logarithmic distance $\rho(n)$. Here, b_c^- marks the start of the chaotic transition, defined as the parameter value where the linear fit of the instantaneous Lyapunov exponent λ first overlaps with $\rho(n)$ within a tolerance ϵ (determined empirically from the data variance). Conversely, b_c^+ corresponds to the transition's completion, where the linear fit diverges from $\rho(n)$ beyond ϵ . Although this approach is heuristic, it effectively quantifies the interplay between the parameter drift rate and the emergence of chaos, offering critical insights into the system's dynamical evolution.

We observe that the chaotic transition starts at lower values of the parameter b_n when the parameter changes more slowly. This is attributed to the fact that a slower change brings us closer to the stationary scenario, where chaos in a region of the phase space is closely tied to the presence of invariant curves. As the growth rate of the parameter increases, we move further away from the stationary scenario, and it takes some time for our system to begin experiencing significant stretching, ultimately leading to chaotic behavior.

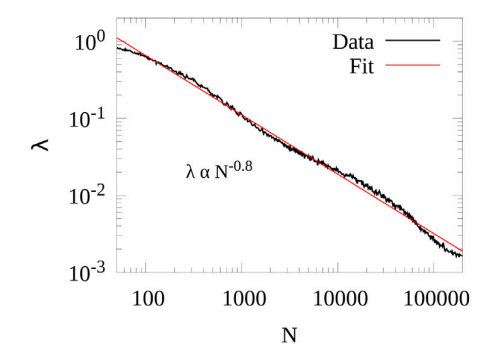
Although the phase space in non-autonomous systems depends on the evolution scenario of the parameter $[b_0,b_f,N]$, the critical parameters for the chaotic transition b_c^- and b_c^+ are associated with the stationary behavior of the system. In a stationary state, only one critical parameter b_c defines the shearless breaking point. The invariant curve is broken once this point is reached, but partial barriers may still exist (see Refs. [17,18]). In a time-dependent system, the transition is smooth and influenced by N.

Fig. 9 shows the scalings between λ and b_c with the total number of iterations for $b_0 = 0$ and $b_f = 2$.

We see that for slower variations of the parameter b_n , the critical parameters b_c have an asymptotic behavior, following the power laws $b_c^- - b_\infty^- \propto N^{-0.6}$ and $b_c^+ - b_\infty^+ \propto N^{-0.5}$, where b_∞^\pm are the asymptotic critical parameters for $N \to \infty$. Here, b_∞^\pm are approximated using large-N simulations (see the magnification in the right panel).

The Lyapunov exponent tends to zero as the number of iterations tends to infinity because, for conservative Hamiltonian systems, a volume element of the phase space will stay the same along a trajectory and remnants of KAM tori hinder transport [15].

Fig. 10 shows the ensemble-averaged pairwise logarithmic distance calculated on the parameter space. We do the following: for each (fixed) value of parameter a, we define the initial condition as points on the shearless curve for $b_0 = 0$, and we iterate it using the NASNM, for each



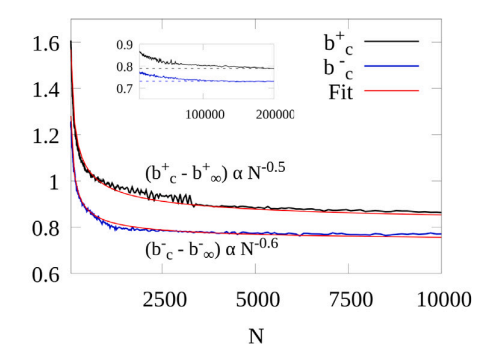


Fig. 9. Scaling for the instantaneous Lyapunov exponent λ and the critical parameter b_c in function of number of iterations N. The dotted lines on the magnification of the right panel show the asymptotic critical parameters.

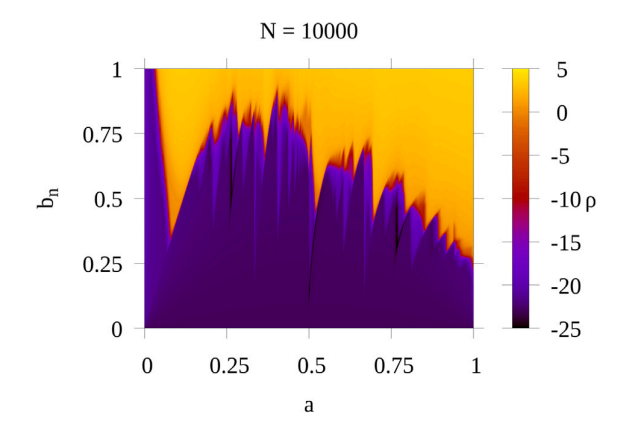


Fig. 10. Parameter space for the non-autonomous SNM. The color scheme represents the ensemble-averaged pairwise logarithmic distance.

instant, we calculate the EAPLD, showed through the color. Although the phase spaces are very different from the static case to the non-autonomous, we see the similarities in the parameter space with the static case (see Ref. [20]).

Fig. 11 shows the transient region $b_c^- < b_n < b_c^+$ for different numbers of iterations. We see that a slower parameter growth rate leads to a sharper transition, closer to the static picture, while a faster parameter growth rate exhibits a smoother transition.

The magnification in Fig. 11 reveals an anomalous broadening of the transient region $b_c^- < b_n < b_c^+$ for specific parameter regimes, such as $a \approx 0.74$, where slower parameter growth (larger N) unexpectedly results in a smoother transition rather than the sharper threshold observed for $a \approx 0.72$. This deviation arises from high-order separatrix reconnection near the shearless curve, a phenomenon amplified at larger N. Prolonged exposure to parameter drift causes the ensemble to deform into a multi-layered tubular structure, significantly expanding its phase-space footprint. Consequently, trajectories near the ensemble's periphery experience enhanced stretching, escaping earlier than they would in compact, reconnection-free scenarios (e.g., $a \approx 0.72$). This premature escape accelerates the onset of chaotic transport, effectively lowering b_a^- and widening the transient region. Such dynamics highlight the delicate interplay between parameter drift rates, separatrix topology, and finite-time ensemble evolution in non-autonomous systems.

As we discussed in Section 1, the SNM is reversible, implying that we can represent the time-reversed map $M^{(-n)}$ as

$$y_n = y_{n+1} + b_n \sin(2\pi x_n),$$

$$x_n = x_{n+1} - a(1 - y_{n+1}^2)$$
(9)

Now let us define the initial state \mathbf{R}_0 as a sequence of points initially on the shearless curve for b_0 . The ensemble evolution is followed through the evolution scenario $[b_0,b_f,N]$, resulting in the final state $\mathbf{R}_N=M^{(N)}(\mathbf{R}_0)$, where we use the notation $M^{(N)}$ to represent N successive iterations of the map M. Then, we reconstruct the initial ensemble by applying the time-reversed NASNM (9), denoted by $\mathbf{R}_{0'}=M^{(-N)}(\mathbf{R}_N)$.

The reversibility error D is measured as the average distance between the points of the initial ensemble \mathbf{R}_0 and the reconstructed initial ensemble $\mathbf{R}_{0'}$:

$$D(\mathbf{R}_0, \mathbf{R}_{0'}) = \langle |\mathbf{r}_{0'} - \mathbf{r}_0| \rangle \tag{10}$$

The reversibility error calculated under different scenarios of parameter evolution provides an additional tool for examining the transition to large-scale chaos in our system. Fig. 12 shows the reversibility error in function of N in three different ranges of the parameter $[b_0,b_f]$: in the first panel we consider the case where small scale chaos is present, in the central panel the parameter range is such that the chaotic transition might occur, depending on the parameter's growth rate and the last panel shows the result for a parameter range such that large-scale chaos is found.

The reversibility error exhibits distinct scaling behaviors determined by the parameter drift scenario (b_0,b_f) . In regimes dominated by smallscale chaos (first panel, Fig. 12), the reversibility error D follows a power-law dependence on N, with numerical precision modulating the error magnitude akin to additive random noise. For systems with lower numerical precision, the reversibility error increases anomalously at large N, likely due to nonlinear phase-space distortions. These distortions arise because lower precision allows the ensemble to sample a broader phase-space region, where nonlinearities dominate the dynamics. For scenarios encompassing a chaotic transition (central panel), the reversibility error correlates with the parameter growth rate: at low N, minimal D reflects incomplete chaotic transitions, allowing partial reconstruction of the initial phase space. Conversely, higher N values induce full transitions to chaos, rendering phase-space reconstruction unfeasible and amplifying D. Here, precision influences D only prior to the transition, magnifying residual noise. In large-scale chaos regimes (last panel). D similarly follows a power-law scaling. but precision ceases to affect the error systematically. This insensitivity arises because, in large-scale chaos, the ensemble's motion resembles an unbiased random motion. While finite precision introduces numerical noise, the system's intrinsic randomness overshadows these perturbations.

6. Transport properties

In this section, we briefly discuss the transport properties of the NASNM. Unlike the SNM with constant parameters, where we see different scenarios of collision/annihilation of periodic orbits leading

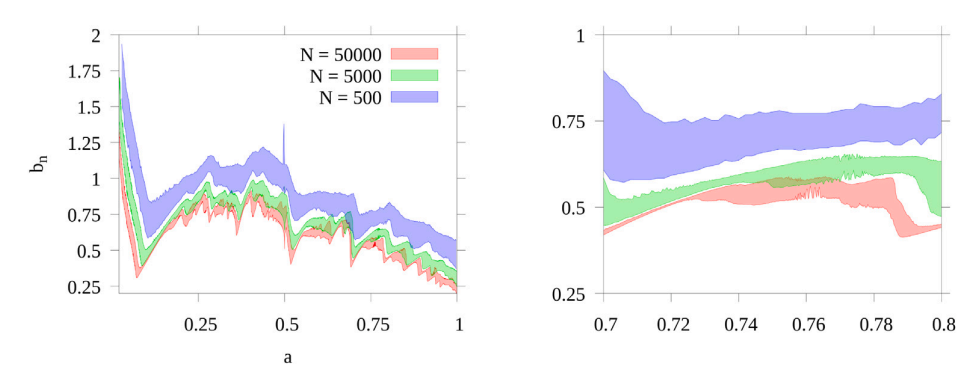


Fig. 11. Transient regions visualized on the parameter space for different numbers of iterations and a magnification in the right panel.

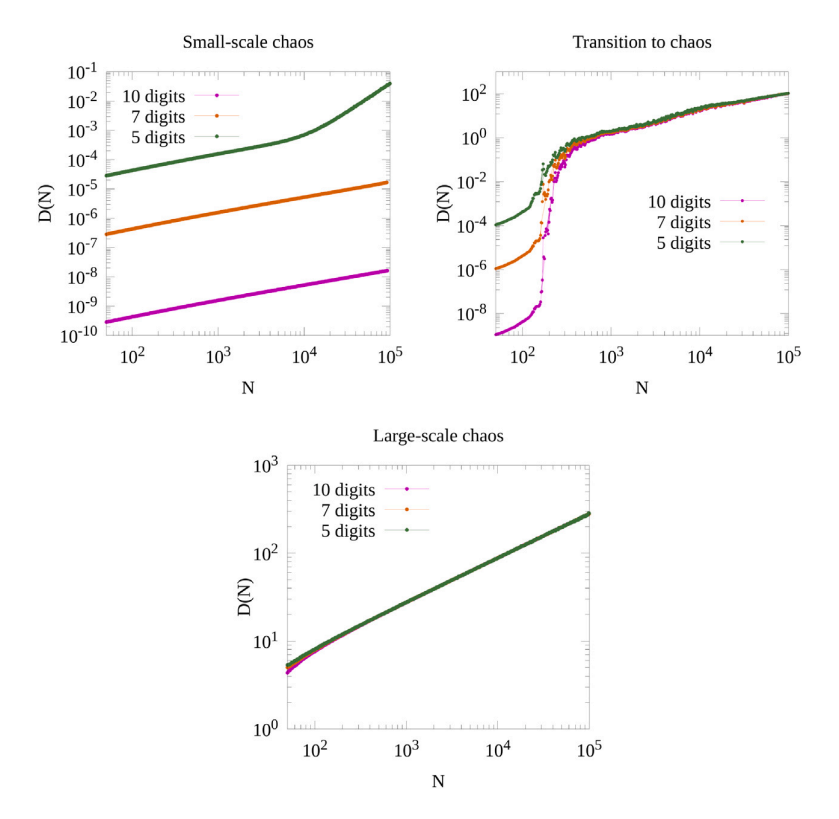


Fig. 12. Reversibility error in function of N in three different scenarios: small-scale chaos corresponds to $[b_0=0,b_f=0.3]$, the intermediate range is $[b_0=0.3,b_f=0.8]$ and finally, large-scale chaos is $[b_0=0.3,b_f=1.8]$. The different colors represent the number of precision digits used for the calculations.

to global transport, depending on the region in the parameter space, for the SNM with time-dependent parameters, the route to chaos is not only related to the two parameters (a,b) but also to the scenario of the evolution of parameter b_n .

We start this section by defining the escape time. The escape time of an orbit (x_n,y_n) is defined as the number of iterations needed to reach a condition of escape $y_n \geq y_{TS}$ in the radial coordinate. Fig. 13 shows the escape time on the phase space for the stationary map and the non-autonomous map with different evolution scenarios of the parameter. The stationary SNM, with the critical parameter $b=b_c=0.83$, and the NASNM, with a fixed total number of iterations N and different scenarios for $[b_0=b_c-\Delta b,b_f=b_c+\Delta b]$, where b_c is the critical parameter for the shearless breaking point in the stationary model.

In the stationary picture, for $b_c=0.83$, the shearless barrier is already destroyed, but we can still see a partial barrier where the shearless curve was previously. We see a region where orbits stay longer, an effect called stickiness.

The non-autonomous map shows a scenario where the region around the shearless barrier also acts as a barrier, as evidenced by the longer escape time within this area. That is because the system preserves a memory of the parameter's evolution. For instance, for $b_0=0.73$, the central barrier still exists on the stationary picture; therefore, orbits in the central region start escaping after the time they would if we start with $b_0=0.83$, where the shearless barrier does not exist anymore on the stationary map.

Let us now consider the average square radial displacement, $\langle \Delta y(n)^2 \rangle$

$$\langle \Delta y(n)^2 \rangle = \langle (y(n) - y(0))^2 \rangle = \frac{1}{NP} \sum_{i=1}^{NP} (y_i(n) - y_i(0))^2,$$
 (11)

where the average is taken over an ensemble of NP points, each ith point located initially at $(x_i(0), y_i(0))$.

Fig. 14 shows the average square radial displacement as a function of n for the stationary SNM, with the critical parameter $b=b_c=0.83$

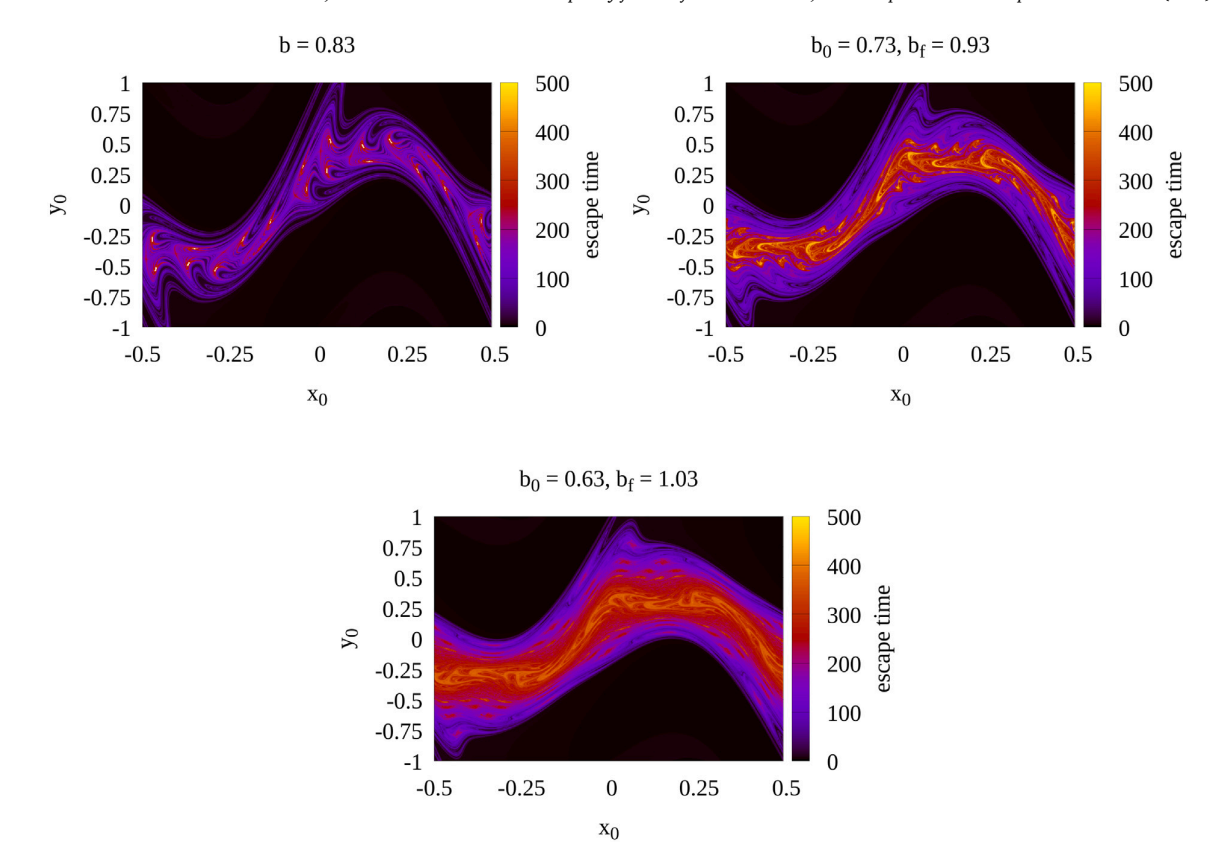


Fig. 13. Escape time distributions across initial phase-space conditions. The first panel shows the stationary system for (b = 0.83). The central and last panels show the non-autonomous systems with $\Delta b = 0.1$ and $\Delta b = 0.2$, resulting in a drift scenario [$b_0 = 0.73$, $b_f = 0.93$] and [$b_0 = 0.63$, $b_f = 1.03$], respectively. Simulations use N = 500 iterations and a radial escape threshold $y_{TS} = 1$.

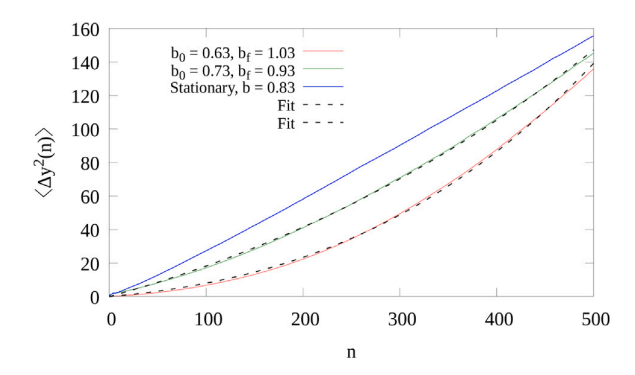


Fig. 14. Average square radial displacement in function of discrete-time n, for an initial ensemble of $NP=10^5$ points located at the horizontal line y=0. The curve in blue represents the static map with $b=b_c=0.83$. The curves in red and green represent the non-autonomous map for $\Delta b=0.2$ and $\Delta b=0.1$, respectively, with N=500. The dotted curves represent fits using the random walk approach with time-increasing steps. (For interpretation of the references to colour in this figure legend, the reader is referred to the web version of this article.)

(blue curve), and the NASNM, with a fixed total number of iterations N=500 and different scenarios for $[b_0=b_c-\Delta b,b_f=b_c+\Delta b]$. The green curve corresponds to $\Delta b=0.1$, resulting in the drift scenario $[b_0=0.73,b_f=0.93]$, while the red curve corresponds to $\Delta b=0.2$, leading to the drift scenario $[b_0=0.63,b_f=1.03]$.

While escape time quantifies the barrier breaking according to a radial displacement threshold y_{TS} , the MSD measures the ensemble-averaged radial spread independently of y_{TS} . These metrics are

complementary but distinct: the former captures directional transport, while the latter characterizes the diffusive behavior. The mean square displacement $\langle \Delta y(n)^2 \rangle$ is calculated for the entire ensemble, irrespective of whether particles exceed y_{TS} .

For the stationary map with $b \geq b_c$ (blue curve in Fig. 14), the destruction of the shearless barrier allows large-scale chaotic transport to dominate the phase space. This regime can be approximated as a two-dimensional random walk with independent time steps. Specifically, in Eq. (1), the variable x_n is treated as a uniformly distributed random variable $\delta \in [-1/2,1/2]$, decoupling it from the radial motion. The radial displacement then simplifies to:

$$y_{n+1} = y_0 - \sum_{i=1}^{n} b \cos(2\pi\delta_i),$$
 (12)

where δ_i represents the stochastic angular displacement at each iteration [21]. For large n, the average square radial displacement for the stationary map converges towards a Gaussian diffusion, and for $b \gg 1$ the correlations between successive values of x_n are reduced, leading to the relation $\langle \Delta y(n)^2 \rangle = (b^2/2)n$.

In the non-autonomous system (red/green curves), the time-dependent parameter b_n introduces time-increasing step sizes to the radial random walk analogy. Here, the radial displacement becomes:

$$y_{n+1} = y_0 - \sum_{i=1}^{n} b_i \cos(2\pi \delta_i), \tag{13}$$

where $b_i = b_0 + iv$ grows linearly with iteration i. Initially ($b_n \le b_c$), large-scale diffusion is suppressed by the shearless barrier, but as b_n exceeds b_c , the shearless curve is broken and the step sizes b_n amplify chaotic transport. This results in a progressive enhancement of $\langle \Delta y(n)^2 \rangle$,

which can be modeled as a random-walk with time-dependent b_i , for which Eq. (13) implies $\langle \Delta y(n)^2 \rangle = \sum_i b_i^2/2$. This effect becomes more pronounced as the system diverges from the static scenario, and by fixing N while taking $\Delta b \to 0$, the static behavior is recovered.

7. Conclusions

This paper introduced the non-autonomous standard nontwist map by considering a drift in parameter b. Conserved quantities and invariant structures, such as KAM tori, are lost for maps with time-dependent parameters. Because of that, we study the system's dynamics by following a set of trajectories that initially start in a single torus of the initial system; in this paper, we followed trajectories initially along the shearless curve. Although there are no invariant structures, we show that the ensemble evolution follows its respective torus in the static map, i.e., the ensemble points are located in the same line in the phase space and have the same rotation number. But after the parameter b_n crosses the separatrix reconnection threshold, the ensemble starts experiencing a strong stretching because the ensemble points are located in a chaotic domain associated with a heteroclinic tangle of the autonomous dynamics.

In the context of non-autonomous systems, the transition to chaos of the shearless barrier was shown to be such that the points of the set initially hardly deviate from each other. The transition begins after a critical value of the parameter b_c^- . During the transition, the points of the set diverge exponentially from each other, with a growth rate of the distances characterized by the instantaneous Lyapunov exponent λ . For b_c^+ , the transition ceases, the distance between the points saturates, and the remnants of the shearless set exhibit chaotic dynamics. Finally, we present power laws relating the parameters λ , b_c^- , and b_c^+ as functions of the total iteration time N. We show the asymptotic behavior of the critical parameters, whereas the instantaneous Lyapunov exponent tends to zero. A second analysis related to the chaotic transition was provided, where we study the distance between the initial condition and the reconstructed initial condition, found by iterating backwards the final state with the time-reversed map. We show that the initial condition can be well reconstructed for a parameter variation scenario where small-scale chaos is found.

Finally, we demonstrate that the parameter drift introduces an additional transport mechanism, altering the diffusion dynamics of the system. In the static case, where $b \geq b_c$, the diffusion is Gaussian and consistent with a random walk characterized by independent steps. For the non-autonomous case, diffusion initially occurs more slowly when the parameter is below the critical threshold. However, as the parameter increases over time, the diffusion is enhanced, leading to greater radial displacements. In analogy to the stationary case, we show that the diffusion properties of the non-autonomous map, for values of b_n large enough, are approximated by the random walk with time-increasing step sizes.

A natural extension of this work lies in exploring parameter drift scenarios bounded by critical thresholds. For systems initialized with $b_0 < b_c$, the time required to breach the shearless barrier inherently depends on N, but further investigations could analyze subcritical cases where both b_0 and b_f remain below b_c . Here, minimal transport is expected due to the intact barrier, though subtle dynamics may arise from the interplay between adiabatic invariance and finite-time parameter drift. Conversely, supercritical scenarios with $b_0, b_f > b_c$ would eliminate the total barrier, enabling studies of how transient memory effects or residual stickiness influence transport even in fully chaotic regimes. Systematic exploration of the drift rate v — particularly its role in modulating chaotic transitions — could delineate critical thresholds where autonomous-like behavior breaks down. For instance, defining bounds on N and $\Delta b = |b_f - b_0|$ that preserve adiabatic invariance (i.e., where dynamics mirror the static case) would offer predictive criteria for phase-space stability. Such scaling laws could unify autonomous and non-autonomous frameworks, bridging gaps in our understanding of time-dependent Hamiltonian systems.

CRediT authorship contribution statement

Marcos V. de Moraes: Writing – original draft, Software, Investigation, Formal analysis. Iberê L. Caldas: Writing – review & editing, Validation, Supervision. Yves Elskens: Writing – review & editing, Validation, Supervision, Formal analysis.

Declaration of competing interest

The authors declare that they have no known competing financial interests or personal relationships that could have appeared to influence the work reported in this paper.

Acknowledgments

The authors thank the financial support from the Brazilian Federal Agencies (CNPq) under Grant Nos. 407299/2018-1, 302665/2017-0, 403120/2021-7, and 301019/2019-3, and the São Paulo Research Foundation (FAPESP, Brazil) under Grant Nos. 2018/03211-6, 2022/04251-7 and 2022/05667-2; and support from Coordenação de Aperfeiçoamento de Pessoal de Nível Superior (CAPES) under Grants No. 88887.710886/2022-00, 88887.522886/2020-00,88881.143103/2017-01 and Comité Français d'Evaluation de la Coopération Universitaire et Scientifique avec le Brésil (COFECUB), Brazil under Grant No. 40273QA-Ph908/18. Centre de Calcul Intensif d'Aix-Marseille is acknowledged for granting access to its high-performance computing resources. YE enjoyed the hospitality of the grupo controle de oscilações at USP.

Data availability

Data will be made available on request.

References

- Lichtenberg AJ, Lieberman MA. Regular and chaotic dynamics. New York: Springer; 1992.
- [2] Lowenstein JH. Essentials of Hamiltonian dynamics. Cambridge: Cambridge University Press; 2012.
- [3] Portela JS, Caldas IL, Viana RL, Morrison P. Diffusive transport through a nontwist barrier in tokamaks. Int J Bifurc Chaos 2007;17(05):1589–98.
- [4] Hazeltine RD, Meiss JD. Plasma confinement. New York: Dover Publications; 2003.
 [5] Ottino JM. The kinematics of mixing: stretching, chaos, and transport, cambridge
- texts in applied mathematics. Cambridge: Cambridge University Press; 1989.

 [6] Pierrehumbert RT. Large-scale horizontal mixing in planetary atmospheres. Phys
- Fluids A Fluid Dyn 1991;3(5):1250–60.

 [7] Kyner WT. Invariant manifolds in celestial mechanics. In: B. D. Tapley V Szebehely, editor. Recent advances in dynamical astronomy. Netherlands, Dordrecht:
- Springer; 1973, p. 192–6. [8] de Sousa MC, Schelin A, Marcus F, Viana RL, Caldas IL. Internal energy exchanges and chaotic dynamics in an intrinsically coupled system. Phys Lett
- A 2022;453:128481.

 [9] Jánosi D, Tél T. Chaos in hamiltonian systems subjected to parameter drift.

 Chaos: An Interdiscip J Nonlinear Sci 2019;29(12):121105.
- [10] Jánosi D, Tél T. Chaos in conservative discrete-time systems subjected to parameter drift. Chaos: An Interdiscip J Nonlinear Sci 2021;31(3):033142.
- [11] Jánosi Dániel, Horváth Anikó, Édes Lili, Kovács Tamás. Magnetic structures in the explicitly time-dependent nontwist map. Chaos: An Interdiscip J Nonlinear Sci 2024;34(12):123160, 12.
- [12] del Castillo-Negrete D, Greene J, Morrison P. Area preserving nontwist maps: periodic orbits and transition to chaos. Phys D: Nonlinear Phenom 1996;91(1-2):1-23.
- [13] del Castillo-Negrete D, Greene J, Morrison P. Renormalization and transition to chaos in area preserving nontwist maps. Phys D: Nonlinear Phenom 1997;100(3):311–29.
- [14] del Castillo-Negrete D, Morrison P. Chaotic transport by rossby waves in shear flow. Phys Fluids A: Fluid Dyn 1993;5(4):948-65.
- [15] Meiss JD. Symplectic maps, variational principles, and transport. Rev Modern Phys 1992;64:795–848.
- [16] Shinohara S, Aizawa Y. Indicators of reconnection processes and transition to global chaos in nontwist maps. Progr Theoret Phys 1998;100(2):219-33.

- [17] Szezech Jr. J, Caldas I, Lopes S, Viana R, Morrison P. Transport properties in nontwist area-preserving maps. Chaos: An Interdiscip J Nonlinear Sci 2009;19(4):043108.
- [18] Szezech Jr. J, Caldas IL, Lopes SR, Morrison P, Viana RL. Effective transport barriers in nontwist systems. Phys Rev E 2012;86(3):036206.
- [19] Jánosi D, Tél T. Overview of the advances in understanding chaos in lowdimensional dynamical systems subjected to parameter drift: Parallel dynamical evolutions and climate change in simple systems. Phys Rep 2024;1092:1-64.
- [20] Wurm A, Apte A, Morrison P. On reconnection phenomena in the standard
- nontwist map. Braz J Phys 2004;34:1700–6.

 [21] Chirikov BV. A universal instability of many-dimensional oscillator systems. Phys Rep 1979;52(5):263–379.